



Effect of gravity on the shape of a droplet on a fiber: Nearly axisymmetric profiles with experimental validation

Ankur Gupta ^{1,3} Andrew R. Konicek,² Mark A. King,² Azmaine Iqtidar ³,
Mohsen S. Yeganeh,² and Howard A. Stone³

¹*Department of Chemical and Biological Engineering, University of Colorado, Boulder, Colorado 80309, USA*

²*ExxonMobil Research and Engineering Company, Annandale, New Jersey 08801, USA*

³*Department of Mechanical and Aerospace Engineering, Princeton University,
Princeton, New Jersey 08544, USA*



(Received 22 February 2021; accepted 3 June 2021; published 21 June 2021)

We study the effect of gravity on barrel-shaped droplets on fibers using theoretical analyses, numerical simulations, and experiments. By performing a perturbation analysis in the limit of small Bond numbers and small dimensionless droplet volumes, we formulate a nearly axisymmetric solution that describes the shape of the droplet. The leading-order solution yields the axisymmetric profile and the first-order correction incorporates the effect of gravity. Thus, we report the droplet shape as a function of dimensionless droplet volume, contact angle, and Bond number. We find that, due to gravity, the contact line position varies sinusoidally with the azimuthal angle around the fiber. We validate our solution by comparing droplet shape and contact line predictions with experiments and numerical simulations.

DOI: [10.1103/PhysRevFluids.6.063602](https://doi.org/10.1103/PhysRevFluids.6.063602)

I. INTRODUCTION

Droplets on fibers are present in a variety of physical systems. In nature, water droplets are commonly observed on tree branches and spider webs. In engineering applications, droplets on fibers are found in filtration, textile, and paper industries. More recently, droplet-on-fiber systems have also been exploited in wire-based microfluidic devices [1–3]. Fundamentally, droplets on fibers are distinct from those on planar surfaces because the presence of an additional length scale (i.e., the fiber radius) impacts the shapes.

Several reports, both experimental and theoretical, have investigated the shape of a single droplet on a fiber. Depending on the contact angle, the fiber radius, and the volume of the droplet, two different fluid morphologies compete with each other: an axisymmetric barrel and an asymmetric clam shell [4,5]. In the limit of negligible gravitational effects, Carroll derived an equation to determine the barrel shape [6] and also proposed a stability criterion [7] to predict the transition between the barrel and clam-shell shapes. Building on Carroll's work, McHale *et al.* [8] and McHale and Newton [9] proposed an improved stability criterion to predict the transition between the two shapes. More recently, by combining experiments and numerical modeling, and by using electrowetting to increase or decrease the *in situ* contact angle, Eral *et al.* [10] showed that the barrel to clam shell and clam shell to barrel transitions, respectively, are governed by different mechanisms. They also developed a detailed phase diagram to identify barrel only, clam shell only, and bistable regions. Chou *et al.* [11] and de Ruiter *et al.* [12] investigated the effect of gravity on the shape of a droplet on a fiber. Specifically, de Ruiter *et al.* [12] studied the effect of gravity on the transition between the two shapes and improved upon the phase diagram proposed by Eral *et al.* [10]. We also

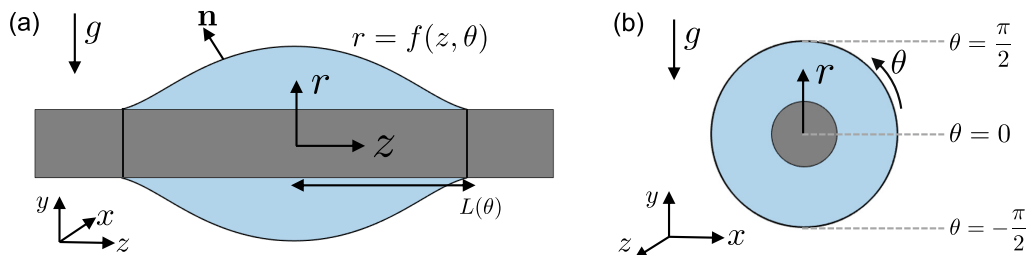


FIG. 1. The barrel-like shape of a drop on a fiber is described as $r = f(z, \theta)$, where z is the axial direction, r is the radial direction, and θ is the azimuthal direction. (a) The front view of the droplet. $z = 0$ plane divides the drop into two symmetric halves. We denote the axial wetted half-length as $L(\theta)$. (b) The end-on view of the droplet. The azimuthal angle $-\pi \leq \theta \leq \pi$, such that $-\pi \leq \theta \leq 0$ and $0 \leq \theta \leq \pi$ denote the bottom portion and top portion of the drop, respectively.

highlight the work by Lorenceau *et al.* where the authors studied the maximal volume of a drop on a horizontal fiber and proposed the condition for detachment of a droplet from a wire [13].

While the aforementioned studies provide a comprehensive understanding of the barrel and the clam-shell shapes, the analyses are focused on the shapes determining the phase space where each conformation exists as a function of dimensionless droplet volume, Bond number, and contact angle. Numerical analyses of the droplet-fiber systems [9–12] are typically achieved using SURFACE EVOLVER [14] simulations. Although numerical simulations provided a better parameter-dependent visualization of the system, the underlying physics of the clam-shell-to-barrel shape transition is still lacking. Therefore, in this research, we make an advancement in the theory to derive the droplet shape and contact line position for a barrel-like droplet in the limit of small Bond numbers and small dimensionless droplet volumes, where the droplet adopts a nearly axisymmetric solution. We note that our approach is similar to the work by Kralchevsky *et al.* [15,16] that focused on the perturbations in the interfacial shape due to interaction with various posts or particles. We validate our results through experiments as well as SURFACE EVOLVER simulations by directly comparing droplet profiles as well as the contact line positions. There are several advantages of our theoretical approach. First, while our analysis focuses on a single droplet and a single fiber, our approach can be useful for more complex physical systems consisting of multiple droplets and fibers [17,18]. Second, the analysis provides a theoretical framework to investigate stability criteria for droplets on fibers while also including the effect of gravity. Finally, our analysis and results can also be adapted for out-of-equilibrium problems dominated by interfacial tension.

II. GENERAL FORMULATION

We use cylindrical coordinates to describe the barrel-shape morphology with r , θ , and z denoting, respectively, the radial, azimuthal, and axial directions. For simplicity, we assume that all the lengths are scaled by the fiber radius a . A plane perpendicular to the z axis, defined here as the $z = 0$ plane, divides the drop into two symmetric halves; see Fig. 1(a). We define the front view to be the projection in the y - z plane. We also define $L(\theta)$ to be the axial wetted half-length; i.e., the surface of the droplet wets the fiber at a distance $L(\theta)$ away to both sides of $z = 0$. We denote the end-on view to be the projection in the x - y plane; see Fig. 1(b). The azimuthal angle $-\pi \leq \theta \leq \pi$, such that $-\pi \leq \theta \leq 0$ and $0 \leq \theta \leq \pi$ denote the bottom portion and top portion of the drop, respectively. In addition, $\beta = \frac{\Delta\rho g a^2}{\gamma}$ is the Bond number, where $\Delta\rho$ is the density difference between the drop and the surrounding fluid, g is the gravitational constant, and γ is the surface tension. We denote V as dimensionless volume (i.e., dimensional volume v scaled such that $V = \frac{v}{a^3}$) and α as the contact angle.

We assume that surface of the barrel-shape droplet is described by $r = f(z, \theta)$, where f is referred to as the shape function. The goal is to determine $f(z, \theta)$ for a given V , α , and β . The mechanical equilibrium is obtained by balancing Laplace pressure and hydrostatic pressure, and the dimensionless form is given by [19]

$$2\mathcal{H} + \beta f \sin \theta = K, \quad (1)$$

where K is a constant that needs to be determined and \mathcal{H} is the dimensionless mean curvature. By definition, $\mathcal{H} = \frac{1}{2} \nabla \cdot \mathbf{n}$, where $\mathbf{n} = n_r \mathbf{e}_r + n_\theta \mathbf{e}_\theta + n_z \mathbf{e}_z$ is the unit normal vector and can be calculated through the gradient of the shape function,

$$n_r = \frac{1}{S}, \quad (2a)$$

$$n_\theta = -\frac{1}{r} \frac{\partial f / \partial \theta}{S}, \quad (2b)$$

$$n_z = -\frac{\partial f / \partial z}{S}, \quad (2c)$$

where $S = \sqrt{1 + \frac{1}{r^2} \left(\frac{\partial f}{\partial \theta} \right)^2 + \left(\frac{\partial f}{\partial z} \right)^2}$. The above leads to

$$2\mathcal{H} = \frac{n_r}{r} + \frac{\partial n_r}{\partial r} + \frac{1}{r} \frac{\partial n_\theta}{\partial \theta} + \frac{\partial n_z}{\partial z}, \quad (3)$$

which along $r = f(z, \theta)$ can be simplified to obtain

$$2\mathcal{H} = \frac{1}{f\Sigma} - \frac{\left[\frac{\partial^2 f}{\partial z^2} \left(1 + \frac{1}{f^2} \left(\frac{\partial f}{\partial \theta} \right)^2 \right) + \frac{1}{f^2} \frac{\partial^2 f}{\partial \theta^2} \left(1 + \left(\frac{\partial f}{\partial z} \right)^2 \right) - \frac{2}{f^2} \frac{\partial f}{\partial \theta} \frac{\partial f}{\partial z} \frac{\partial^2 f}{\partial \theta \partial z} - \frac{1}{f^3} \left(\frac{\partial f}{\partial \theta} \right)^2 \right]}{\Sigma^3}, \quad (4)$$

where $\Sigma = \sqrt{1 + \frac{1}{f^2} \left(\frac{\partial f}{\partial \theta} \right)^2 + \left(\frac{\partial f}{\partial z} \right)^2}$. Equations (1) and (4) can be combined to obtain a partial differential equation for $f(z, \theta)$. The symmetry boundary conditions are

$$\left. \frac{\partial f}{\partial z} \right|_{z=0} = 0, \quad \text{for all } \theta, \quad (5)$$

$$\left. \frac{\partial f}{\partial \theta} \right|_{\theta=-\pi/2, \pi/2} = 0, \quad \text{for all } z. \quad (6)$$

The contact line boundary condition is stated as

$$f(z = L(\theta)) = 1, \quad \text{for all } \theta. \quad (7)$$

Additional constraints are needed to determine K and $L(\theta)$. First, we invoke the contact angle boundary condition, or

$$\mathbf{n} \cdot \mathbf{e}_r|_{z=L(\theta)} = n_r|_{z=L(\theta)} = \frac{1}{\Sigma} \Big|_{z=L(\theta)} = \cos \alpha, \quad \text{for all } \theta. \quad (8)$$

Finally, to complete the formulation, we require a (dimensionless) constant volume constraint, or

$$V = 2 \int_{-\pi/2}^{\pi/2} \int_0^{L(\theta)} (f^2 - 1) dz d\theta. \quad (9)$$

The above set of equations can be evaluated numerically to determine the shape function $f(z, \theta)$. However, given the numerical complexity in solving the aforementioned equations for any set of parameters, we instead focus on the limit of small Bond numbers, or $\beta \ll 1$.

III. THE NEARLY AXISYMMETRIC SOLUTION

Since the condition $\beta = 0$ results in an axisymmetric solution, we seek a nearly axisymmetric solution in the limit $\beta \ll 1$. In this limit, we assume the following expansions:

$$f(z, \theta) = f_0(z) + \beta f_1(z) \sin \theta + O(\beta^2), \quad (10a)$$

$$\Sigma(z, \theta) = \Sigma_0(z) + \beta \Sigma_1(z) \sin \theta + O(\beta^2), \quad (10b)$$

$$K = K_0 + O(\beta^2), \quad (10c)$$

$$L(\theta) = L_0 + \beta L_1 \sin \theta + O(\beta^2), \quad (10d)$$

$$\mathcal{H}(z, \theta) = \mathcal{H}_0(z) + \beta \mathcal{H}_1(z) \sin \theta + O(\beta^2), \quad (10e)$$

where we have assumed that the azimuthal dependence in the first-order correction is proportional to $\sin \theta$. This assumption is motivated by the fact that the gravitational term in Eq. (1) is proportional to $\sin \theta$. Also, to make the first-order balance $O(\beta)$ homogeneous, we assume that K does not have an $O(\beta)$ term. We note that Eq. (10) is valid for $V = O(1)$. However, as we show later, this approximation yields a reasonably accurate result even for larger volumes.

Substituting Eq. (10) into Eqs. (1) and (4) yields the following leading-order, i.e., $O(1)$, balance:

$$\frac{1}{f_0 \Sigma_0} - \frac{d^2 f_0 / dz^2}{\Sigma_0^3} = K_0, \quad (11)$$

where $\Sigma_0 = \sqrt{1 + (df_0/dz)^2}$. Physically, the first term on the left-hand side in Eq. (11) is the out-of-plane curvature whereas the second term is the in-plane curvature. These terms are equivalent to the equations derived by Carroll *et al.* [6] and McHale *et al.* [8].

The first-order balance, i.e., $O(\beta)$, reveals (see the Appendix for the derivation)

$$-\frac{\frac{df_0}{dz} \frac{df_1}{dz}}{f_0 \Sigma_0^3} - \frac{\frac{d^2 f_1}{dz^2}}{\Sigma_0^3} + 3 \frac{\frac{d^2 f_0}{dz^2} \frac{df_0}{dz} \frac{df_1}{dz}}{\Sigma_0^5} + f_0 = 0. \quad (12)$$

The boundary condition at $z = 0$ are simply

$$\left. \frac{df_0}{dz} \right|_{z=0} = 0, \quad (13a)$$

$$\left. \frac{df_1}{dz} \right|_{z=0} = 0. \quad (13b)$$

The boundary condition at the contact line, i.e., $f(L(\theta)) = 1$, can be written as

$$f(L_0 + \beta L_1 \sin \theta) = 1. \quad (14)$$

After applying a Taylor series expansion, Eq. (14) becomes

$$f(L_0) + \beta L_1 \sin \theta \left. \frac{df_0}{dz} \right|_{z=L_0} = f_0(L_0) + \beta \left(f_1(L_0) \sin \theta + L_1 \left. \frac{df_0}{dz} \right|_{z=L_0} \sin \theta \right) = 1, \quad (15)$$

and, applying the balances at $O(1)$ and $O(\beta)$, these boundary conditions become

$$f_0(L_0) = 1, \quad (16a)$$

$$f_1(L_0) + L_1 \left. \frac{df_0}{dz} \right|_{z=L_0} = 0. \quad (16b)$$

Similarly, the contact angle boundary condition, Eq. (8), i.e., $\frac{1}{\Sigma} \Big|_{L(\theta)} = \cos \alpha$, becomes

$$\left. \frac{\partial f}{\partial z} \right|_{z=(L_0+\beta L_1)} = -\tan \alpha. \quad (17)$$

TABLE I. Summary of $O(1)$ and $O(\beta)$ equations and boundary conditions for the nearly axisymmetric solution.

| $O(1)$ balance solve $f_0(z)$, L_0 , and K_0 | $O(\beta)$ balance solve $f_1(z)$ and L_1 |
|--|---|
| $\frac{1}{f_0 \Sigma_0} - \frac{d^2 f_0 / dz^2}{\Sigma_0^3} = K_0; \Sigma_0 = \sqrt{1 + (df_0 / dz)^2}$ $\frac{df_0}{dz} \Big _{z=0} = 0$ $f_0(L_0) = 1$ $\frac{df_0}{dz} \Big _{L_0} = -\tan \alpha$ $V = 2\pi \int_0^{L_0} (f_0^2 - 1) dz$ | $-\frac{df_0}{f_0 \Sigma_0^3} \frac{df_1}{dz} - \frac{d^2 f_1}{dz^2} + 3 \frac{d^2 f_0}{dz^2} \frac{df_0}{dz} \frac{df_1}{dz} + f_0 = 0$ $\frac{df_1}{dz} \Big _{z=0} = 0$ $f_1(L_0) + L_1 \frac{df_0}{dz} \Big _{z=L_0} = 0$ $\frac{df_1}{dz} \Big _{z=L_0} + L_1 \frac{d^2 f_0}{dz^2} \Big _{z=L_0} = 0$ |

Again applying a Taylor series expansion to Eq. (17) and applying the balances at $O(1)$ and $O(\beta)$ yield

$$\frac{df_0}{dz} \Big|_{L_0} = -\tan \alpha, \quad (18a)$$

$$\frac{df_1}{dz} \Big|_{z=L_0} + L_1 \frac{d^2 f_0}{dz^2} \Big|_{z=L_0} = 0. \quad (18b)$$

The volume conservation equation can be stated as

$$V = 2 \int_{-\pi/2}^{\pi/2} \int_0^{L_0 + \beta L_1 \sin \theta} (f^2 - 1) dz d\theta, \quad (19)$$

which can be shown to lead to

$$V = 2\pi \int_0^{L_0} (f_0^2 - 1) dz + O(\beta^2). \quad (20)$$

We summarize the final equations and boundary conditions for $O(1)$ and $O(\beta)$ in Table I.

IV. RESULTS FROM THE NEARLY AXISYMMETRIC SOLUTION

For given V and α , the ordinary differential equations in Table I are solved numerically to evaluate $f_0(z)$, $f_1(z)$, L_0 , L_1 , and K . The shape function is evaluated as $f(z, \theta) = f_0(z) + \beta f_1(z) \sin \theta$ and the contact line position is evaluated as $(r, \theta, z) = (1, \theta, L_0 + \beta L_1 \sin \theta)$. We summarize the results in Fig. 2 for $V = 125$ and $\alpha = \frac{\pi}{12}$.

The results demonstrate the effect of gravity on the droplet shape; see Figs. 2(a)–2(c). When viewed from the front (y - z plane) and end-on (x - y plane), our results shows that the asymmetry due to the effect of gravity increases as β increases, as would be expected on physical grounds. It is also useful to view the changes in contact line position due to gravity. Without gravity ($\beta = 0$ case), the contact line position does not depend on θ and the contact line is a circle with the same radius as that of fiber. Therefore, when viewed from the top looking in the direction of gravity, the contact line appears to a straight line; see Fig. 2(a). However, when gravitational effects are included, the contact lines shorten on the upper side and lengthen on the lower portion of the fiber; see Figs. 2(b) and 2(c). As per our model, the dependence of this movement is proportional to β and is sinusoidal with θ ; see Fig. 2(d).

V. EXPERIMENTAL AND SIMULATION DETAILS

Experiments were conducted to validate the theoretical results. A custom-built apparatus was designed that would hold a cylindrical glass fiber at the eucentric point of a camera attached to

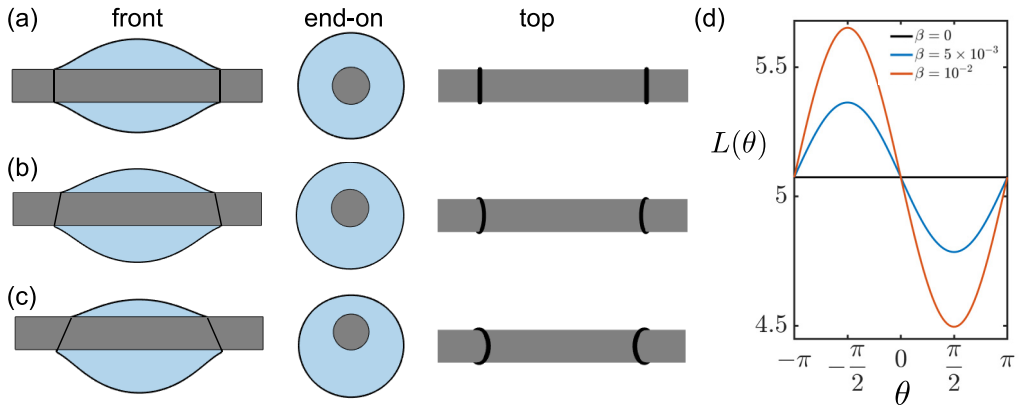


FIG. 2. The nearly axisymmetric solution as described in Table I. Front (x - y plane) and end-on views (y - z plane) of the droplet for $V = 125$, $\alpha = \frac{\pi}{12}$, and (a) $\beta = 0$, (b) $\beta = 5 \times 10^{-3}$, and (c) $\beta = 10^{-2}$. The contact line as viewed from the top looking in the direction of gravity is also provided. (d) The axial wetted half length, i.e., $L = L_0 + \beta L_1 \sin \theta$ for $V = 125$ and $\alpha = \frac{\pi}{12}$.

a goniometer; see Fig. 6. The fiber is held horizontally with the length running orthogonal to gravity. Next, the fiber is carefully aligned as any slight tilt of the fiber can cause the droplet to skew or even move. Also mounted to the goniometer, on the opposite side of the camera, is a $2'' \times 2''$ white collimated LED backlight (Metaphase Technologies, part 14-270). This backlight floods the camera's contrast and produces a two-dimensional shadow-cast image of the fiber and droplet profile.

The fibers in these experiments are glass microcapillaries of various diameters (128, 221, 600 μm). Each fiber has the diameter measured with a caliper before each experiment. Fibers were plasma treated to achieve a 0-deg contact angle with the wetting fluid, polyalphaolefin (PAO4) with density 819 kg/m^3 and surface tension 28 mN/m . PAO4 droplets were added using a micropipette on the lowest volume setting (VWR Ultra High-Performance). A small amount of volume was produced by partially depressing the pipette plunger and that fractional volume was transferred to the microcapillary by contact. This was in an attempt to deposit volumes less than 1.0 μL and as low as 0.1 μL . While this method does not control how much volume is deposited, the amount that does wet the fiber can be calculated from the subsequent data analysis. After the droplet is placed, the goniometer is rotated and images are taken every 5 deg.

Raw images are first analyzed to align them with the center of the fiber and center of the droplet. An edge detection routine is used to obtain the entire profile of the fiber-air and liquid-air interfaces for all images. The edge of the fiber-air interface is used to rotate, align, and center all images. This rotation and translation is performed on the raw image data and then the edge detection is run again (to avoid propagating any errors) to generate a final stack of images. The pixel width of the unwetted fiber is determined by taking the mode of all diameters from all images. That value, along with the caliper measurement of the fiber, is used to calculate the distance per pixel in the image series and then generate the three-dimensional data set of the entire fiber and droplet surface. From that data set, the droplet volume, contact line position, and droplet profiles are generated.

In addition, we utilize SURFACE EVOLVER to perform numerical simulations. We modify the code provided in Chapter 8 of Ref. [20] to obtain shape profiles. To ensure that our simulation setup is accurate, we benchmark our results in the absence of gravity using the analytical results of Carrol [6] and the experimental data of Eral *et al.* [10].

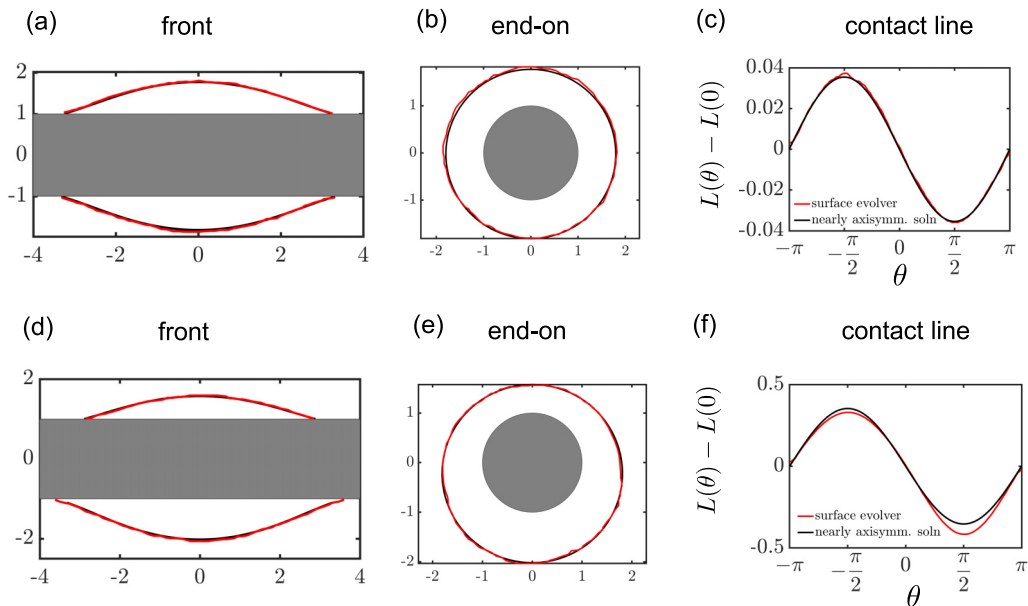


FIG. 3. Comparison of nearly axisymmetric solution with SURFACE EVOLVER simulations for $V = 27$, $\alpha = \frac{\pi}{12}$, and [(a)–(c)] $\beta = 10^{-3}$ and [(d)–(f)] $\beta = 10^{-2}$. The black lines represent the nearly axisymmetric solution and the red lines represent the SURFACE EVOLVER simulations. Comparisons of the front view (y - z plane), end-on view (x - y plane), and contact line position $[L(\theta) - L(0)]$ are provided.

VI. VALIDATION WITH SURFACE EVOLVER SIMULATIONS

We first validate our results with SURFACE EVOLVER simulations; see Fig. 3. Here, we compare the results for $\alpha = \frac{\pi}{12}$, $V = 27$, and $\beta = 10^{-3}$ [Figs. 3(a)–3(c)] and $\beta = 10^{-2}$ [Figs. 3(d)–3(f)]. We find that the proposed nearly axisymmetric solution is in excellent agreement with the SURFACE EVOLVER simulations for both these conditions and is able to reproduce the front view, the end-on view, and the contact line position. We highlight that even though our model was developed for $V = O(1)$, it works reasonably well for $V = 27$. However, we note that for $\beta = 10^{-2}$, SURFACE EVOLVER simulations display a minor asymmetry in the contact line position [see Fig. 3(f)], an effect that is not captured in the nearly axisymmetric solution.

VII. VALIDATION WITH EXPERIMENTS

We summarize the direct comparisons of shape profiles and contact lines in Fig 4. In Figs. 4(a)–4(c), the experimental data relates to the condition where the droplet volume is $1.3 \mu\text{L}$, fiber radius $a = 110.5 \mu\text{m}$, and contact angle $\alpha = 0$. Therefore, $V = 962$ and $\beta = 3.5 \times 10^{-3}$, which were used for the nearly axisymmetric calculations and SURFACE EVOLVER simulations. The results display a good quantitative agreement between the three approaches, as evident from the front and end-on view comparisons; see Figs. 4(a) and 4(b). The contact line position data is also in qualitative agreement and shows a sinusoidal behavior with θ , consistent with our prediction. To further validate our results, we also compared a system with droplet volume $0.92 \mu\text{L}$, $a = 300 \mu\text{m}$, and $\alpha = 0$; see Figs. 4(d)–4(f). Therefore, $V = 34$ and $\beta = 2.49 \times 10^{-2}$. Similar to the previous result, we observe good quantitative agreement for the front and end-on views between the three approaches, and the contact line displays a sinusoidal dependence with θ .

We emphasize that while our perturbation result has been derived for $V = O(1)$, it is able to predict the front and end-on views with reasonable quantitative accuracy. However, there is quantitative

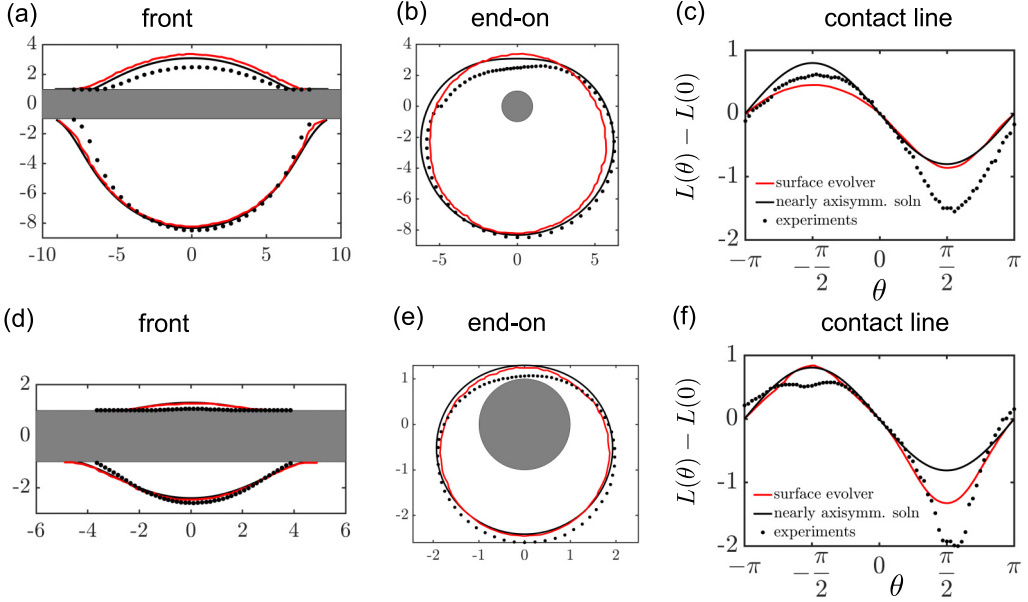


FIG. 4. Validation of nearly axisymmetric solution with experiments and SURFACE EVOLVER simulations. (a) Front view (y - z plane), (b) end-on view (x - y plane), and (c) the half-wetted length, i.e., $L(\theta) - L(0)$ for $V = 962$, $\alpha = 0$, and $\beta = 3.5 \times 10^{-3}$. (d) Front view, (e) end-on view, and (f) $L(\theta) - L(0)$ for $V = 34$, $\alpha = 0$, and $\beta = 2.49 \times 10^{-2}$. Black circles are experimental data, the black lines are nearly axisymmetric solutions, and the red lines are SURFACE EVOLVER simulations.

disagreement between experiments and the models in predicting contact line position, especially for $L(\theta)$ when $\theta > 0$. To a lesser extent, this disagreement is also seen in SURFACE EVOLVER simulations. To check whether this trend is consistent, we conducted additional experiments with $a = 64 \mu\text{m}$ ($\beta = 1.16 \times 10^{-3}$), droplet volumes $0.59 \mu\text{L}$ ($V = 2274$) and $0.97 \mu\text{L}$ ($V = 3695$), and $\alpha = 0$; see Fig. 5. The disagreement between experiments and the nearly axisymmetric solutions for $\theta > 0$ is also observed for these additional conditions.

One of the factors that leads to a greater disagreement in contact line positions for larger Bond numbers and volumes is the tendency of the droplet to adopt a clam-shell-like shape and eventually detach from the fiber. As detailed by de Ruiter *et al.* [12], the physical mechanism

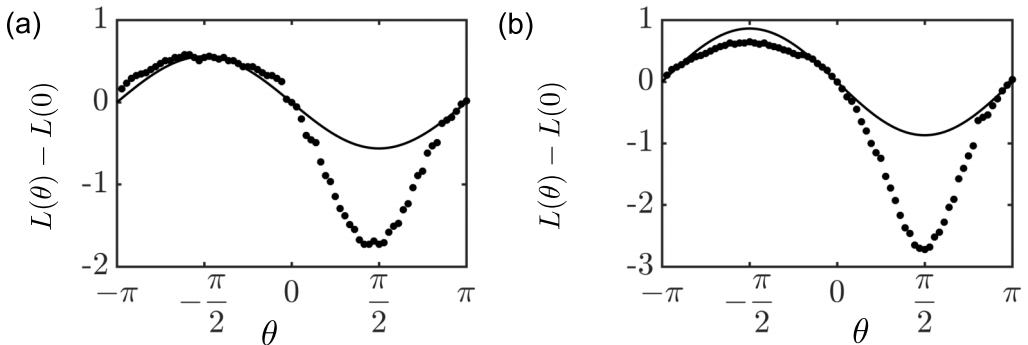


FIG. 5. Comparison of contact line from experiments (circular data points) and nearly axisymmetric solution (solid line) for (a) $V = 2274$ and (b) $V = 3695$. $\beta = 1.16 \times 10^{-3}$, and $\alpha = 0$.

that results in these transitions is the liquid neck that forms on top of the fiber and subsequently ruptures. The condition for droplet detachment roughly follows $\beta_v = \frac{\Delta\rho g v^{2/3}}{\gamma} = O(1)$; see Fig. 3 in Ref. [12]. The experimental data provided represents $\beta_v = 0.34$ [Figs. 4(a)–4(c)], $\beta_v = 0.26$ [Figs. 4(d)–4(f)], $\beta_v = 0.20$ [Fig. 5(a)], and $\beta_v = 0.28$ [Fig. 5(b)]. While these conditions do not result in detachment, the volumes are large enough for the asymmetry to appear in $L(\theta)$ for $\theta > 0$. In fact, the experimental data in Figs. 4 and 5 support this assessment since the contact line shapes resemble a neck. The nearly axisymmetric solution is unable to capture the necking instability since the former assumes a small deviation from the axisymmetric solution. Mathematically, the expansions listed in Eq. (10) are no longer sufficient to capture this asymmetry. We note that while the SURFACE EVOLVER simulations presented here predict asymmetry in the contact line [see Fig. 4(f)], they are also unable to completely capture the necking feature. This disagreement occurs because to achieve necking in the SURFACE EVOLVER simulations, it is crucial to perturb the system parameters such as contact angle and center-of-mass position, as has been discussed in Refs. [10,11,20].

In addition, while the models use $\alpha = 0$ based on planar contact angle measurements, the experimental images of the fiber suggest that the apparent contact angle might be nonzero. Nonetheless, the solution is still able to reproduce the front and end-on views observed in experiments. More importantly, it provides insights into the movement of the contact line position and the effect of gravity that are otherwise difficult to infer from numerical simulations.

VIII. CONCLUSION

In this research, we conducted a regular perturbation analysis for a single drop wetting a fiber to capture the effect of gravity on barrel-like droplet shapes and the contact line position. The final equations for the nearly axisymmetric solution are summarized in Table I. Our equations are able to capture the effect of gravity on droplet shape and suggest that the contact line position is sinusoidal with azimuthal angle θ . We validated our results with equivalent experiments and SURFACE EVOLVER simulations, and obtained qualitative agreement with the experiments and quantitative agreement with the simulations.

While the results in this research describe the scenario of a single droplet on a fiber, the approach can be extended to more complicated wetted systems. For instance, our approach is applicable to a droplet wetting multiple fibers, where the structure of the perturbation expansion will be similar but the boundary conditions and the volume conservation equations will need to be appropriately modified. In addition, our approach can also be useful for droplet-fiber systems that are out of equilibrium and where the effect of gravity may be important.

ACKNOWLEDGMENT

We thank ExxonMobil Research and the Andlinger Center for Energy and the Environment at Princeton University for funding.

APPENDIX

1. Derivation of $O(\beta)$ balance

Here, we present the derivation $O(\beta)$ balance provided in Eq. (12). We start by recalling that

$$f(z, \theta) = f_0(z) + \beta f_1(z) \sin \theta + O(\beta^2). \quad (\text{A1})$$

Substituting Eq. (A1) in the expression of $\Sigma = \sqrt{1 + \frac{1}{f^2} \left(\frac{\partial f}{\partial \theta} \right)^2 + \left(\frac{\partial f}{\partial z} \right)^2}$, we write

$$\Sigma = \sqrt{1 + \left(\frac{df_0}{dz} \right)^2 + 2\beta \frac{df_0}{dz} \frac{df_1}{dz} \sin \theta + O(\beta^2)}. \quad (\text{A2})$$

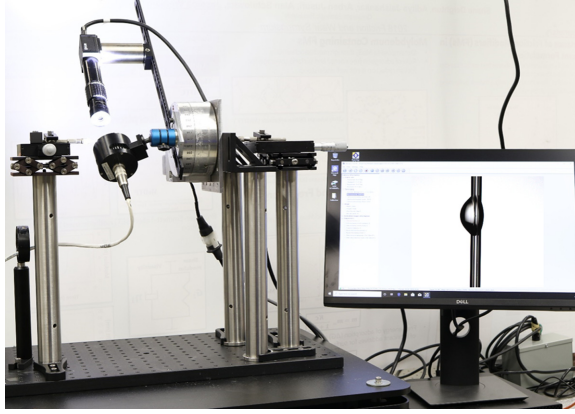


FIG. 6. Image of our experimental setup.

By applying binomial approximation on Eq. (A2), we obtain

$$\Sigma = \Sigma_0 + \beta \Sigma_1 \sin \theta + \dots, \quad (\text{A3})$$

where

$$\Sigma_0 = \sqrt{1 + \left(\frac{df_0}{dz}\right)^2}, \quad (\text{A4a})$$

$$\Sigma_1 = \frac{\frac{df_0}{dz} \frac{df_1}{dz}}{\Sigma_0}. \quad (\text{A4b})$$

Substituting Eqs. (A1) and (A3) in the first term of the right-hand side of Eq. (4) and utilizing the binomial expansion, we get

$$\frac{1}{f\Sigma} = \frac{1}{f_0\Sigma_0} - \beta \sin \theta \left(\frac{f_1}{f_0^2\Sigma_0} + \frac{\Sigma_1}{f_0\Sigma_0^2} \right) + O(\beta^2). \quad (\text{A5})$$

Similarly, substituting Eqs. (A1) and (A3) in the second term of the right-hand side of Eq. (4) and utilizing the binomial expansion, we get

$$\begin{aligned} & \frac{\left[\frac{\partial^2 f}{\partial z^2} \left(1 + \frac{1}{f^2} \left(\frac{\partial f}{\partial \theta} \right)^2 \right) + \frac{1}{f^2} \frac{\partial^2 f}{\partial \theta^2} \left(1 + \left(\frac{\partial f}{\partial z} \right)^2 \right) - \frac{2}{f^2} \frac{\partial f}{\partial \theta} \frac{\partial f}{\partial z} \frac{\partial^2 f}{\partial \theta \partial z} - \frac{1}{f^3} \left(\frac{\partial f}{\partial \theta} \right)^2 \right]}{\Sigma^3} \\ &= -\frac{\frac{d^2 f_0}{dz^2}}{\Sigma_0^3} - \beta \sin \theta \left(\frac{\frac{d^2 f_1}{dz^2}}{\Sigma_0^3} - \frac{f_1}{f_0^2 \Sigma_0} - \frac{3\Sigma_1 \frac{d^2 f_0}{dz^2}}{\Sigma_0^4} \right) + O(\beta^2). \end{aligned} \quad (\text{A6})$$

Combining Eqs. (4), (A5), and (A6) yields

$$2\mathcal{H} = 2\mathcal{H}_0 + 2\beta\mathcal{H}_1 \sin \theta + O(\beta^2), \quad (\text{A7})$$

where

$$2\mathcal{H}_0 = \frac{1}{f_0 \Sigma_0} - \frac{\frac{d^2 f_0}{dz^2}}{\Sigma_0^3} \quad (\text{A8})$$

and

$$2\mathcal{H}_1 = -\frac{\Sigma_1}{f_0 \Sigma_0^2} - \frac{\frac{d^2 f_1}{dz^2}}{\Sigma_0^3} + \frac{3\Sigma_1 \frac{d^2 f_0}{dz^2}}{\Sigma_0^4}. \quad (\text{A9})$$

By utilizing Eq. (A4b), we can write

$$2\mathcal{H}_1 = -\frac{\frac{df_0}{dz} \frac{df_1}{dz}}{f_0 \Sigma_0^3} - \frac{\frac{d^2 f_1}{dz^2}}{\Sigma_0^3} + 3 \frac{\frac{d^2 f_0}{dz^2} \frac{df_0}{dz} \frac{df_1}{dz}}{\Sigma_0^5}. \quad (\text{A10})$$

To obtain the result described in Eq. (12), we note that $2\mathcal{H}_1 + f_0 = 0$.

2. Experimental setup

An image of our experimental set up is provided in Fig. 6.

-
- [1] T. Gilet, D. Terwagne, and N. Vandewalle, Digital microfluidics on a wire, *Appl. Phys. Lett.* **95**, 014106 (2009).
 - [2] T. Gilet, D. Terwagne, and N. Vandewalle, Droplets sliding on fibres, *Eur. Phys. J. E* **31**, 253 (2010).
 - [3] S. Dorbolo, D. Terwagne, N. Vandewalle, and T. Gilet, Resonant and rolling droplet, *New J. Phys.* **10**, 113021 (2008).
 - [4] N. Adam, Detergent action and its relation to wetting and emulsification, *J. Soc. Dyers Colour.* **53**, 121 (1937).
 - [5] P.-G. De Gennes, F. Brochard-Wyart, and D. Quéré, *Capillarity and Wetting Phenomena: Drops, Bubbles, Pearls, Waves* (Springer Science & Business Media, Berlin, 2013).
 - [6] B. Carroll, The accurate measurement of contact angle, phase contact areas, drop volume, and Laplace excess pressure in drop-on-fiber systems, *J. Colloid Interface Sci.* **57**, 488 (1976).
 - [7] B. Carroll, Equilibrium conformations of liquid drops on thin cylinders under forces of capillarity. A theory for the roll-up process, *Langmuir* **2**, 248 (1986).
 - [8] G. McHale, N. Káb, M. Newton, and S. M. Rowan, Wetting of a high-energy fiber surface, *J. Colloid Interface Sci.* **186**, 453 (1997).
 - [9] G. McHale and M. Newton, Global geometry and the equilibrium shapes of liquid drops on fibers, *Colloids Surf., A* **206**, 79 (2002).
 - [10] H. B. Eral, J. de Ruiter, R. de Ruiter, J. M. Oh, C. Semperebon, M. Brinkmann, and F. Mugele, Drops on functional fibers: From barrels to clamshells and back, *Soft Matter* **7**, 5138 (2011).
 - [11] T.-H. Chou, S.-J. Hong, Y.-E. Liang, H.-K. Tsao, and Y.-J. Sheng, Equilibrium phase diagram of drop-on-fiber: Coexistent states and gravity effect, *Langmuir* **27**, 3685 (2011).
 - [12] R. de Ruiter, J. de Ruiter, H. B. Eral, C. Semperebon, M. Brinkmann, and F. Mugele, Buoyant droplets on functional fibers, *Langmuir* **28**, 13300 (2012).
 - [13] É. Lorenceau, C. Clanet, and D. Quéré, Capturing drops with a thin fiber, *J. Colloid Interface Sci.* **279**, 192 (2004).
 - [14] K. A. Brakke, The surface evolver, *Exp. Math.* **1**, 141 (1992).
 - [15] P. Kralchevsky, V. Paunov, N. Denkov, I. Ivanov, and K. Nagayama, Energetical and force approaches to the capillary interactions between particles attached to a liquid-fluid interface, *J. Colloid Interface Sci.* **155**, 420 (1993).
 - [16] P. A. Kralchevsky, V. N. Paunov, N. D. Denkov, and K. Nagayama, Capillary image forces: I. Theory, *J. Colloid Interface Sci.* **167**, 47 (1994).
 - [17] A. Sauret, F. Boulogne, B. Soh, E. Dressaire, and H. A. Stone, Wetting morphologies on randomly oriented fibers, *Eur. Phys. J. E* **38**, 62 (2015).
 - [18] A. Sauret, F. Boulogne, D. Cébron, E. Dressaire, and H. A. Stone, Wetting morphologies on an array of fibers of different radii, *Soft Matter* **11**, 4034 (2015).
 - [19] W. M. Deen, *Analysis of Transport Phenomena* (Oxford University Press, New York, 2012).
 - [20] J. Berthier and K. A. Brakke, *The Physics of Microdroplets* (John Wiley & Sons, New York, 2012).